Molecular-scale simulation of cross-flow migration in polymer melts

Nicholas A. Rorrer and John R. Dorgan*

Department of Chemical and Biological Engineering, Colorado School of Mines, 1500 Illinois Street, Golden, Colorado 80401, USA

(Received 25 June 2014; revised manuscript received 10 November 2014; published 24 November 2014)

The first ever molecular-scale simulation of cross-flow migration effects in dense polymer melts is presented; simulations for both unentangled and entangled chains are presented. At quiescence a small depletion next to the wall for the segmental densities of longer chains is present, a corresponding excess exists about one-half a radii of gyration away from the wall, and uniform values are observed further from the wall. In shear flow the melts exhibit similar behavior as the quiescent case; a constant shear rate across the gap does not induce chain length based migration. In contradistinction, parabolic flow (where gradients in shear rate are present) causes profound migration for both unentangled and entangled melts. Mapping onto polyethylene and calculating stress shows the system is far below the stress required to break chains. Accordingly, our findings are consistent with flow induced migration mechanisms predominating over competing chain degradation mechanisms thus resolving a 40 year old controversy.

DOI: 10.1103/PhysRevE.90.052603 PACS number(s): 83.80.Sg, 83.10.Rs, 83.50.Ha

I. INTRODUCTION

Chain-length dependent migration effects due to shear rate (or stress) gradients are of fundamental scientific interest. Technologically, the phenomenon is important in polymer processing [1,2], flow in porous media [3], and next generation DNA sequencing technologies [4–6]. Cross flow migration is thought to be influenced by many factors ranging from chain stiffness and enthalpic interactions to geometric effects, the type of flow field, and wall-slip phenomena. Despite the importance of the phenomenon, it is difficult to obtain *in situ* measurements of length-based migration. The combined fundamental interest, technological importance, and experimental difficulties provide a strong motivation for studying the issue using molecular-scale simulations.

To date, molecular simulations have focused on migration effects in dilute polymer solutions with an emphasis on DNA [7–11] These studies present differing results—showing migration towards the center of the channel or the wall depending on the potentials adopted and simulation technique used. Dissipative particle dynamics have predicted migration towards the walls [7] while Brownian dynamics and some molecular dynamics treatments find migration to the midplane [9–11]. Khare *et al.* [11] attempted to clear up some of the confusion in the literature on solutions by attributing migration to three different mechanisms: wall interactions, thermal diffusion, and gradients in chain mobility. There are just a few simulation studies of segregation effects in dense polymer melts and these are limited to bidisperse melts at reduced densities [12,13]; only one of these studies incorporates flow effects [13]. Similarly, while theoretical developments have progressed for dilute solutions [14–16], results are sparse for melts [17,18]. Despite the fundamental interest and technological importance, no simulation studies on polydisperse melts have appeared in the literature, presumably due to the computational complexity.

While relatively little attention has been paid to migration behavior in polymer melts in recent years, there is a long history regarding the phenomena. Busse [19,20] noted the possibility and proposed that shear rate gradients create an entropic driving force that leads to segregation of high molecular weights away from the walls. Early experiments by Segre and Silverberg on two phase flow [21] were followed by investigation of melts by Schreiber, Storey, and Bagley [22,23]. Molecular weight measurements on linear polyethylene samples extruded through dies of differing lengths showed that the extrudate skin was of lower molecular weight than the core. In contradistinction, Whitlock and Porter [24,25] performed experiments on polystyrene and only observed a low molecular weight skin at high shear rates and elevated temperatures leading them to conclude that the lower molecular weight at the interface is a result of thermomechanical degradation. Subsequently, Lee and White [26,27] used a capillary rheometer to show that in mixtures of high and low density polyethylene, the higher viscosity HDPE migrates to the core. In addition, for miscible mixtures of low and high molecular weight polystyrene these same researchers found an excess of low molecular weight material on their extrudate exteriors. In a much more recent study Musil and Zatloukal [28] study die "drool" during polymer extrusion; the die drool phenomena corresponds to an accumulation of polymer material at the die face (i.e., at the "lip"). These authors also report that the die drool material possesses a lower molecular weight than the rest of the extrudate and that its formation directly precedes flow instabilities. Likewise Inn has reported migration effects in bimodal molecular weight distributions of metallocene-based polyethylenes in capillary rheology [29]. In summary, despite its fundamental nature and technological importance, the experimental literature is not conclusive regarding the role of length-based migration versus chain degradation.

II. METHODOLOGY

The present study investigates dense polydisperse polymer melts on a lattice using the COMOFLO algorithm [30,31] which is a variant of the COMOTION algorithm of Pakula

*Author to whom correspondence should be addressed: jdorgan@mines.edu

[32]. This highly efficient technique enables the simulation of coarse grained polymer melts on a face-centered-cubic lattice at full density (volume fraction, $\varphi = 1.0$). In the present study the chains are held between two hard walls (surface interaction parameter, $\chi_s = 0$). Algorithmic moves are designed to mimic the conformational rearrangements of polymer chains. The implementation of polydispersity [33], shear flow [30], and parabolic flow [31] have been successfully demonstrated. In addition, the algorithm accurately captures polymer dynamics [30] and wall-slip phenomena [34].

A. Mapping of the lattice to real space and time

The COMOFLO algorithm running on a face-centered-cubic lattice can be mapped onto any real polymer melt. Here the physical system adopted is polyethylene due to its prevalence and the large amount of available literature data. From a first principles perspective, it is important to understand that the lattice beads do not have an inherent mass so the usual MLt (mass, length, time) system of dimensions is not usually used but the perfectly equivalent FLt (force, length, time) system is naturally suited for polymeric systems. In addition, as shown below it is possible to assign a mass to each bead when this is desired (for example when calculating the Reynolds number).

1. Length scale matching—the end-to-end vector

In order to map the simulation length scale (that is, the lattice spacing) to real polymer length scales, the end-to-end vector connecting the first and last segment of a polymer chain is utilized. For the model applied to monodisperse linear chains it is found that the equilibrium ensemble averaged root mean squared end-to-end vector [32], $\langle R^2\rangle^{1/2}$, scales as: [35]

$$\langle R^2\rangle^{1/2}\, 1.58N^{0.5}, \tag{1}$$

where N is the total number of chain segments and the length is measure in lattice units (mcs - Monte Carlo sites). The r.m.s. end-to-end vector can be measured for any real polymer; for polyethylene the ratio of the mean squared radius of gyration ($\langle s^2\rangle$) divided by the molecular weight is relatively independent of temperature [36] and this result can be recast into the expression for the end-to-end vector given by Eq. (2):

$$\langle R^2\rangle^{1/2}\, 5.76N^{0.5}. \tag{2}$$

In Eq. (2), the units of length are Angstroms and the number of segments N is the number of repeating ethylene groups. By equating Eqs. (1) and (2), the length of a lattice unit is determined. In this case, where the mapping is onto polyethylene, each lattice site is equivalent to 3.65 Å. The mapping of the end-to-end vector establishes a real physical length scale in Angstroms.

As mentioned, this length matching associates each lattice site with an ethylene repeat unit. Using this same association of an ethylene group per lattice site and matching an experimental value for the melt density of polyethylene of 0.866 g/cm^3 at 140 °C gives a similar value of 3.77 Å. Accordingly while the matching is imperfect, it is reasonable and fully consistent with a lattice spacing corresponding to 3.71 +/− 0.06 Å/mcs and a segmental mass corresponding to polyethylene (28.06 g/mol).

2. Time scales—from Rouse to reptation dynamics

To calculate velocity profiles and the dynamic correlation functions, a fundamental time step must be assigned. Time steps are assigned to algorithmic moves that mimic conformation isomerization of polymer chains. Following Mansfield and Theodorou [37] the fundamental time step, t_u, is defined as,

$$t_u = 1/N_{\text{Total Segments}}, \tag{3}$$

where $N_{\text{Total Segments}}$ is the total number of segments on the lattice (the number of chains times the segments per chain, N). If n_{moves} is the number of Monte Carlo moves, when $t_u * n_{\text{moves}} = 1$ then on average each segment in the box has experienced an attempted displacement. (In molecular dynamics simulations each particle also experiences an "attempted move" as a result of the forces imposed). Time is incremented by t_u for each local movement completed. These local moves include end bond rotations, crankshaft-like motions around two bonds, kink straightening or formation and displacement of a few segments along the chain contour. Full details of these elementary moves is outlined in the sixth chapter of Ref. [38].

Using the above time scheme, the COMOFLO algorithm is capable of reproducing proper dynamics of polymer melts. Dynamics are probed by calculating a set of correlation functions that monitor the movement of specific segments in the polymer chain as a function of time. In these correlation functions the position of the ith segment is monitored as a function of time ($r_i(t)$). Some of the correlation function are monitored relative to the position of the center of mass, $r_{\text{cm}}(t)$. The first correlation function, $g_1(t)$, monitors the displacement of the central segment and is given by

$$g_1(t) = \langle [r_i(t) - r_i(t=0)]^2\rangle \quad \text{for} \quad i = \frac{N}{2}. \tag{4}$$

The $g_2(t)$ correlation function monitors the displacement of the central segment relative to the center of mass and is given by

$$g_2(t) = \langle \{[r_i(t) - r_{\text{cm}}(t)] - [r_i(t=0) - r_{\text{cm}}(t=0)]\}^2\rangle \quad \text{for} \quad i = \frac{N}{0}. \tag{5}$$

The $g_3(t)$ correlation function monitors the displacement of the center of mass and is given by

$$g_3(t) = \langle [r_{\text{cm}}(t) - r_{\text{cm}}(t=0)]^2\rangle. \tag{6}$$

The $g_4(t)$ correlation function monitors the displacement of the chain ends (first and last segment) and is given by

$$g_4(t) = \langle [r_i(t) - r_i(t=0)]^2\rangle \quad \text{for} \quad i = 1 \quad \text{and} \quad N. \tag{7}$$

Finally the $g_5(t)$ correlation function monitors the displacement of the chain ends relative to the first center of mass and is given by

$$g_5(t) = \langle \{[r_i(t) - r_{\text{cm}}(t)] - [r_i(t=0) - r_{\text{cm}}(t=0)]\}^2\rangle \quad \text{for} \quad i = 1 \quad \text{and} \quad N. \tag{8}$$

Polymer chains below the critical molecular weight for entanglement follow Rouse dynamics. For Rouse dynamics the g_1, g_2, g_4, and g_5 correlation functions scale as t^1 at short times and as $t^{1/2}$ at intermediate times. At long times the g_1

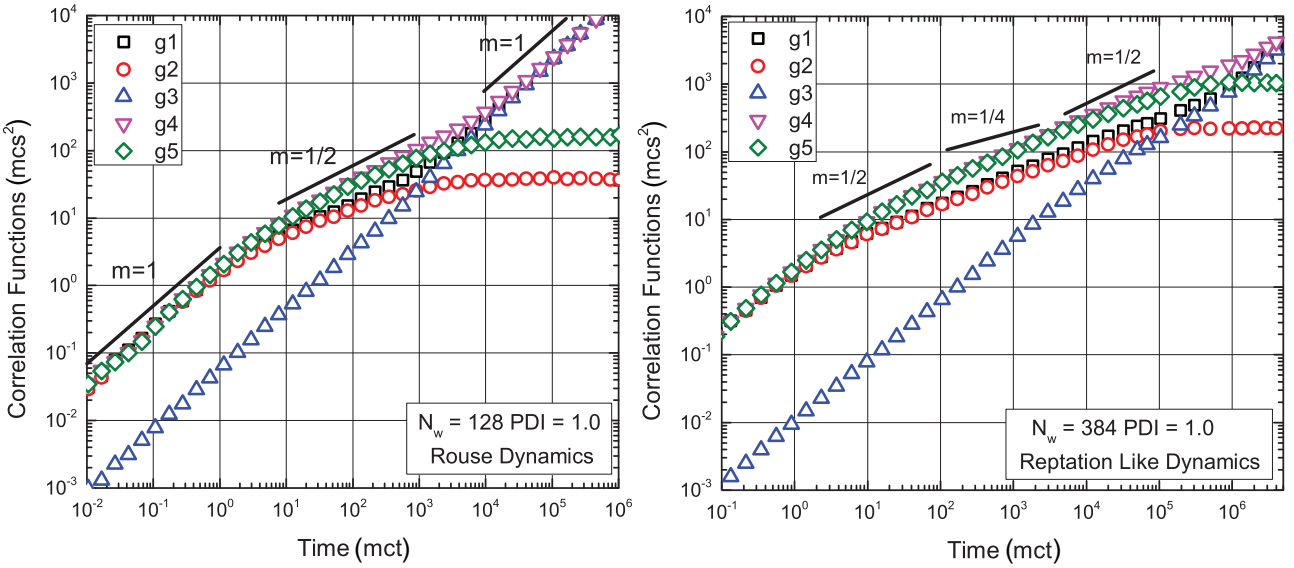

FIG. 1. (Color online) The five correlation functions for an $N_w = 128$ (left) and $N_w = 384$ (right) monodisperse system (PDI = 1.0). The hallmark $t^{1/4}$ scaling is present in the entangled melt.

and g_4 correlation functions scale as t^1 and the g_2 and g_4 scale as t^0. Figure 1 demonstrates these different scaling regimes for a monodisperse $N = 128$ system.

The transition from Rouse to reptationlike dynamics indicates the transition from unentangled to entangled polymer melts. For reptation dynamics the g_1, g_2, g_4, and g_5 the correlation function scales as $t^{1/2}$ for times below the entanglement time, τ_e. The hallmark scaling of reptation dynamics occurs at short time between the entanglement and Rouse time, τ_R, and the g_1, g_2, g_4, and g_5 correlation functions scale as $t^{1/4}$. Above the Rouse time and between the disengagement times, the g_1, g_2, g_4, and g_5 the correlation function scales as $t^{1/2}$. Finally, at long times, above disengagement time, the g_1 and g_4 correlation functions scale as t^1 and the g_2 and g_5 scale as t^0. An example of the reptationlike dynamic signature is also provided in Fig. 1.

In previous work [30,33], the present algorithm has demonstrated its ability to capture the crossover from Rouse dynamics to reptationlike dynamics just by increasing chain length for both monodisperse and polydisperse polymer melts. This crossover occurs at a critical chain length of N_c of approximately 100 segments.

It is also important to note that the $g_3(t)$ correlation function scales as $6Dt$ at long times. This provides the method for matching time scales between the simulation and real polymer systems. An example of this long time behavior is provided in Fig. 2. The measured self-diffusivities of polyethylene [39] provide a means to map mct to real time.

Center of mass motion simulation data (from the $g3$ correlation function) for a $N = 128$ fully periodic system (without walls) versus time is analyzed. A linear data fit between 10^5 and 6×10^5 Monte Carlo time (mct) steps has a slope of 5.78×10^{-3} (mcs^2/mct) (with a regression coefficient of 0.999). Using the lattice spacing determined above, this value becomes 7.7×10^{-18} (cm^2/mct). This slope is set equal to six times the self-diffusion coefficient for an oligomeric polyethylene having a molecular weight of $M = NM_o = 128$ (segments) $\times$ 28 [(g/mol)/segment] = 3584 g/mol. To find the self-diffusivity of the real molecule, the experimental result summarized by Eq. (9) is used, [39],

$$D_{\text{self}} = \frac{18.7}{M^{2.3}}\left(\frac{\text{cm}^2}{\text{s}}\right). \tag{9}$$

Equation (9) is valid for a reference temperature of 140 °C and gives a value of 1.25×10^{-7} (cm^2/s) for $M =$ 3584 (g/mol); six times this value is 7.50×10^{-7} (cm^2/s). Equating this later value with the simulation value of 7.7×10^{-18} (cm^2/mct) provides 1.0×10^{-11} (s/mct). If the analysis is repeated for different N values (from 16 upwards) this same order of magnitude is always found.

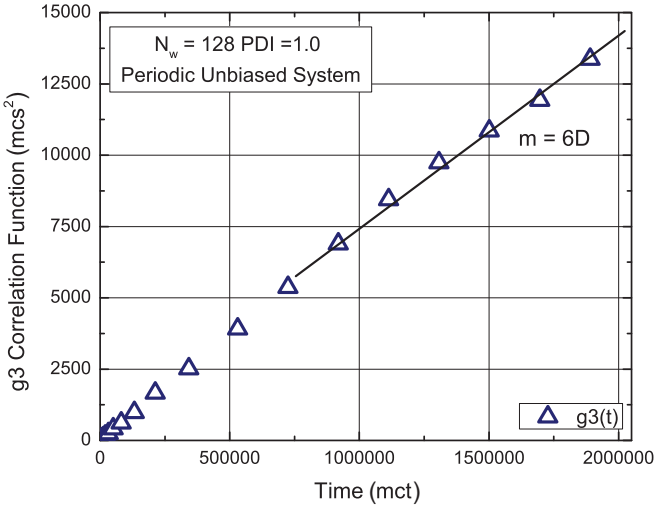

FIG. 2. (Color online) An example of the long time behavior of the g_3 correlation function for the $N = 128$ case showing linear behavior at long times. The slope of the long time behavior, m, is equal to 6 times the self-diffusion coefficient.

The simulations are able to access shear rates of 10^{-7} (1/mct) and still reliably extract viscosities meaning simulations corresponding to real shear rates as low as 10^{-4} (1/s) are possible; this is one order of magnitude lower than the best coarse grained molecular dynamics (MD) simulations and 10 to 11 orders of magnitude lower than the typical MD simulations on slip and other flow phenomena presented in the literature.

3. Mapping viscosity and stress

In the simulations a dimensionless stress tensor $\underline{\underline{\sigma}}$ is utilized and is calculated according to Eq. (10),

$$\frac{\underline{\underline{\sigma}}}{2\nu kT} = \frac{3\underline{r}\,\underline{r}}{2\langle R^2\rangle_0}, \tag{10}$$

where k is Boltzmann's constant, T is temperature, ν is the number of strands per unit volume, $\langle R^2\rangle_0$ is the mean squared end-to-end vector under unperturbed conditions, and $\langle \underline{r}\,\underline{r}\rangle$ is the dyadic product of the bond vectors.

Stress can be assigned physical values by matching values of the zero shear viscosity to experimental systems. In the simulations, entangled polymer melts of chain length $N = 256$ possess a zero shear viscosity of 3.1 (Π mct) where Π indicates dimensionless stress units. Given the previous mapping, the corresponding molecular weight is calculated as 7.2 kg/mol, which is above the critical molecular weight for entanglement of polyethylene ($M_c = 3.8$ kg/mol). Regardless of polydispersity, entangled polymer melts possessing the same weight average molecular weight possess the same zero shear viscosity. It is also known that the zero shear viscosity scales as the weight average molecular weight to the 3.4 power ($\eta_0 \sim N^{3.4}$). Using the experimental data provided in Jordens *et al.* [40] and extrapolating to a molecular weight of 7.2 kg/mol (corresponding to the $N = 256$ case) results in a zero shear viscosity of 0.543 Pa s. Equating the experimental value to the simulation value gives a viscosity conversion factor of 0.175 (Pa s)/(Π mct). Applying the conversion factor between mct and real time of 1.0×10^{-11} (s/mct) gives 1.75×10^{10} Pa/Π. Equivalently, shear stress σ_{xy} can be expressed as the product of the shear viscosity η and shear rate $\dot{\gamma}$,

$$\sigma_{xy} = \eta\dot{\gamma}. \tag{11}$$

By dividing the real shear stress $\sigma_{xy,\text{real}}$ by the simulation shear stress $\sigma_{xy,\text{sim}}$ one arrives at the following relationship:

$$\frac{\sigma_{xy,\text{real}}}{\sigma_{xy,\text{sim}}} = \frac{\eta_{\text{real}}}{\eta_{\text{sim}}}\frac{\dot{\gamma}_{\text{real}}}{\dot{\gamma}_{\text{sim}}}. \tag{12}$$

The simulation shear rate can be expressed in terms of the real shear rate, using the previous time scale conversion as

$$\dot{\gamma}_{\text{sim}}\left(\frac{1}{\text{mct}}\right) = \dot{\gamma}_{\text{real}}\left(\frac{1}{\text{s}}\right)t_{\text{conversion}}\left(\frac{\text{s}}{\text{mct}}\right) = 10^{-11}\dot{\gamma}_{\text{real}}. \tag{13}$$

Substituting Eq. (12) into Eq. (11) and using the viscosity conversion, the shear stress conversion is again

$$\frac{\sigma_{xy,\text{real}}}{\sigma_{xy,\text{sim}}} = \frac{\eta_{\text{real}}}{\eta_{\text{sim}}}\frac{\dot{\gamma}_{\text{real}}}{\dot{\gamma}_{\text{real}} \times 10^{-11}} = 1.75 \times 10^{10}\ \text{Pa}/\Pi. \tag{14}$$

TABLE I. Summary of conversion for polyethylene melts.

Unit	Conversion
Length	3.77 Å/mcs
Time	1.0×10^{-11} s/mct
Mass	28.06 g/(mol segments)
Velocity	37.7 (m/s)/(mcs/mct)
Viscosity	0.175 Pa s/Π mct
Stress	1.75×10^{10} Pa/Π

Table I provides a summary of the conversion factors for mapping the fcc lattice model onto polyethylene chains in real space and time.

4. Reynolds and Weissenberg numbers

In order to calculate the Reynolds number all units are converted from the simulation units into real world units. Recall that the Reynolds number, Re, is defined as

$$\text{Re} = \frac{\rho\langle v\rangle L}{\eta}. \tag{15}$$

Consistent with the mapping of real space, $\rho = 886$ kg/m^3 is used for the density, L is the plate spacing, $\langle v\rangle$ is the average velocity across the grap, and η is the viscosity. By using the previously outlined conversions, three decades in the Reynolds number are obtained, ranging 10^{-5}–10^{-2}, for the systems studied. Such values are physically reasonable for typical polymer melt processes.

In the context of this model the Weissenberg number Wi is defined as

$$\text{Wi} = \dot{\gamma}\lambda, \tag{16}$$

where $\dot{\gamma}$, is taken to be the wall shear rate in the simulations, and λ is the longest relaxation time. In this case the ensemble averaged τ_R is determined from the scaling of the correlation function. In these simulations the dimensionless Weissenberg number spans three decades from 0.1 to 10.

B. Variables used to characterize segregation

Different metrics can be used to describe chain segregation. The segmental density $\rho_{\text{seg},i}(x)$ is averaged for each chain length i as a function of box position and is defined as

$$\rho_{\text{seg},i}(x) = \frac{ns_i(x)}{ns_{i,T}/L}, \tag{17}$$

where $ns_i(x)$ is the number of segments in an x plane belonging to chain i and $ns_{i,T}$ is the total number of segments belonging to chains of type i in the simulation. L is the spacing between the hard walls so that when segments are uniformly distributed, the defined density is unity. An excess gives a value higher than 1 and depletion corresponds to values less than 1. To demonstrate the enhancement of segmental densities under flow conditions, the ratio defined by Eq. (18) is used,

$$\tilde{\rho}_{\text{seg},i}(x) = \frac{\rho_{\text{seg},i}(x)[\text{Flow}]}{\rho_{\text{seg},i}(x)[\text{No Flow}]}. \tag{18}$$

The apparent wall shear rate $\dot{\gamma}_A$ is determined from the flow rate $\dot{Q}$ through the channel following the usual rheological protocol [41] by utilizing Eq. (19),

$$\dot{\gamma}_A = \frac{6\dot{Q}}{WL^2}, \tag{19}$$

where W is the width in the transverse direction.

III. RESULTS AND DISCUSSION

Results for both unentangled and entangled chains are reported. Unentangled polymer melts with $N_w = 64$ and $N_n = 44$ (consisting of 313 chains: 86 of $N = 16$, 91 of $N = 32$, 127 of $N = 64$, 7 of $N = 129$, and 2 of $N = 256$) were simulated at a plate spacing of 48 segments. In the entangled case, results for a five chain system with corresponding weight average chain length with $N_w = 256$ segments (analogous to the weight average molecular weight, M_w). Entanglement in the model begins at about $N = 100$ and is evident for $N = 128$ for a monodisperse system [30]. The plates are spaced at 128 lattice units apart corresponding to about ten radii of gyration for the average chain length. Periodic boundary conditions are applied in the other directions. The total number of chains is 1520; 469 of $N = 64$, 471 of $N = 128$, 496 of $N = 496$, 80 of $N = 512$, and 4 of $N = 1024$. Details of equilibration and flow implementation are available in earlier references [30,31,35]. Results for the unentangled case closely parallel the results for the entangled case; one distinction is that for entangled chains wall slip provides a slight shear rate gradient near the wall which is absent in the unentangled case (see velocity profiles).

A. Velocity profiles

Data for both unentangled and entangled systems are presented including the velocity profiles associated with the steady-state flows. Details of the flow biasing methodology have been presented in earlier publications [30,31]. When no biasing is applied, the system is quiescent whereas spatially dependent biasing can produce either plane shear (Couette) or parabolic (Poiseulle) flow. Briefly, to simulate flow in the y direction, the random walk of segmental displacements must be biased. To accomplish this biasing, a position in the box, x div, is defined as

$$x_{\text{div}} = \frac{x}{nx+1} - \frac{1}{2}, \tag{20}$$

where nx is the number of lattice segments between the hard walls in the x direction. This coordinate gives x div as $-1/2$ at the left wall, $1/2$ at the right, and zero at the middle. To implement shear flow, the probabilities of taking a step in the forward, p_{+y}, and backward direction, p_{-y}, respectively are

$$p_{+y} = p_{\text{zero}} - p_{\max} x_{\text{div}}, \tag{21}$$

$$p_{-y} = p_{\text{zero}} + p_{\max} x_{\text{div}}, \tag{22}$$

$$p_y = p_{\text{zero}}, \tag{23}$$

where p_{zero} is the probability of making a move in any direction with no biasing present (i.e., $p_{\text{zero}} = 1/3$) and $p_{\max}$ is the biasing parameter that sets the flow strength. The sum of the probabilities for motion is unity as they include $p_y = p_{\text{zero}}$ corresponding to lateral motion. To implement parabolic flow, Eqs. (24)–(26) are implemented,

$$p_{+y} = p_{\text{zero}} + p_{\max}[1 - (2x_{\text{div}})^2], \tag{24}$$

$$p_{-y} = p_{\text{zero}} - p_{\max}[1 - (2x_{\text{div}})^2], \tag{25}$$

$$p_y = p_{\text{zero}}. \tag{26}$$

In either case, when $p_{\max}$ is zero then $p_{+y} = p_{-y} = p_y = p_{\text{zero}} = 1/3$ is recovered and no flow occurs.

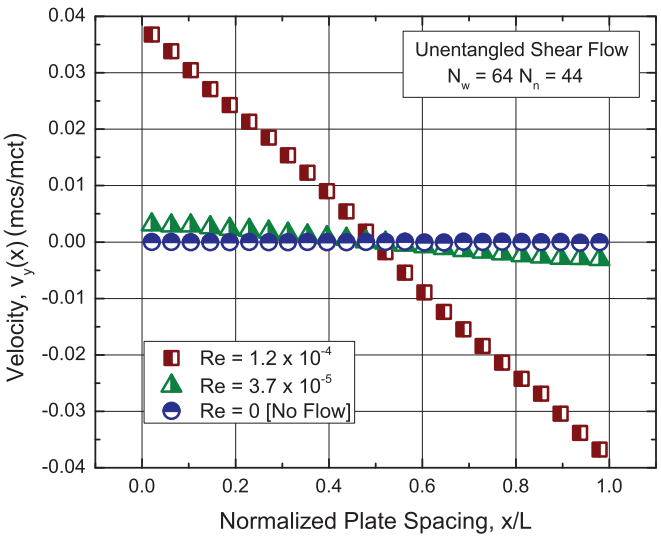

FIG. 3. (Color online) Velocity profiles for unentangled melt in shear flow. Unlike entangled melts, even at higher Re numbers, slip is not present so there is no shear rate gradient.

Figure 3 presents velocity profiles for the unentangled $N_w = 64$ melt in shear flow. Unlike entangled melts, even at high Re numbers, slip is not present so there is no shear rate gradient in the near wall region. In contrast, Fig. 4 provides velocity profiles for the same unentangled melt undergoing parabolic flow; at the higher Re numbers studied, significant wall slip is present. A layer having a thickness of approximately the average radius of gyration is pulled along the wall by the flowing melt.

Figures 5 and 6 present analogous velocity profiles for the higher molecular weight, $N_W = 256$, melt. Figure 5 shows the shear flow result; compared to the unentangled melt, slip is clearly present at a Reynolds number which is an order of magnitude lower. Such a finding is consistent with the broad consensus that slip is prevalent in high molecular weight systems [42,43].

B. Segmental distributions

Even in the absence of flow, the introduction of hard walls creates deviations from a uniform distribution of segmental densities. Figures 7 and 8 present the segmental densities as a function of spacing for no flow conditions; there is a near-wall depletion of segments from the longer chains and slight near-wall enhancement of segments belonging to shorter chains. Near the center of the box, segmental densities are nearly uniform but show some effects of confinement due to

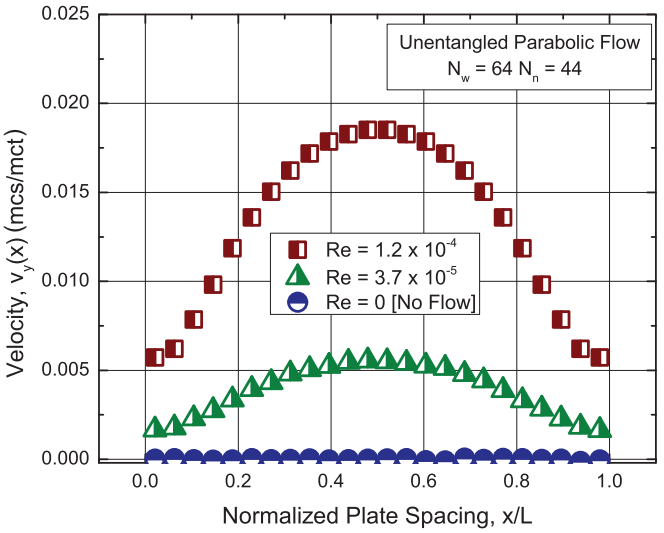

FIG. 4. (Color online) Velocity profiles for unentangled parabolic flow. Unlike shear flow, at high Re numbers, significant slip is present. Even when the slip velocity is modest, migration is profound as shown in Fig. 13.

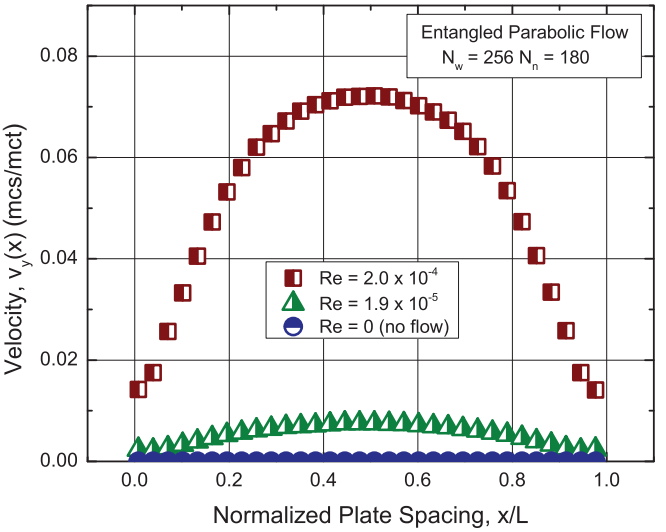

FIG. 6. (Color online) Velocity profiles for entangled parabolic flow. As with shear flow, at high Re numbers, slip is present. However, even for cases of minimal wall slip, migration is profound as shown in Fig. 14.

the width of the box being only 10 average radii of gyrations. These simulation results agree with field theories based on entropic arguments [44,45]—chain ends are preferred near the reflecting walls because the perturbation of equilibrium chain conformations are minimized.

Under simple shear flow (linear velocity field) the segmental density distributions are very similar to the quiescent case. This is shown in Figs. 9 and 10. In Figure 9, unentangled data is presented at a shear rate of 2.5×10^{-4} mct^{-1} which corresponds to a physical shear rate of 2.5×10^{7} (1/s). These simulations are at high shear rates and yet *almost no additional migration other than that caused by the walls is evident*. At even higher shear rates when slip and cohesive failure are present [34], additional migration can occur but this is accompanied by velocity banding, that is, by an inhomogeneous shear rate. The data of Figures 9 and 10 compared to that of Figs. 7 and 8 enable the conclusion that simple homogeneous shear does not lead to chain-length based migration in polymer melts.

Poiseulle flow (where there is a parabolic velocity field across the gap) is very different from simple shear with respect to chain migration effects. When gradients in shear rate are present, polymer melts exhibit strong flow migration phenomena. For unentangled chains, Fig. 11 demonstrates that at a wall shear rate comparable to the shear flow of Fig. 9, migration is clearly present. Equivalently for entangled

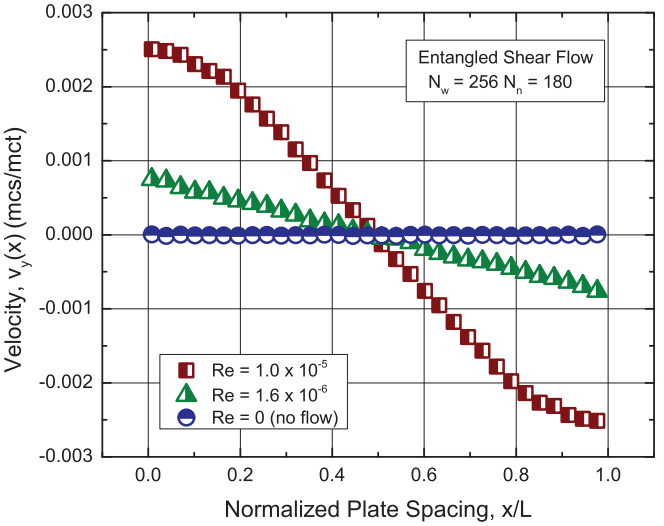

FIG. 5. (Color online) Velocity profiles for entangled shear flow. At Re numbers of 10^{-5}, wall slip is present which provides a shear rate gradient. This small shear rate gradient explains the deviation from no flow conditions in the segmental densities with increasing Re shown in Fig. 14.

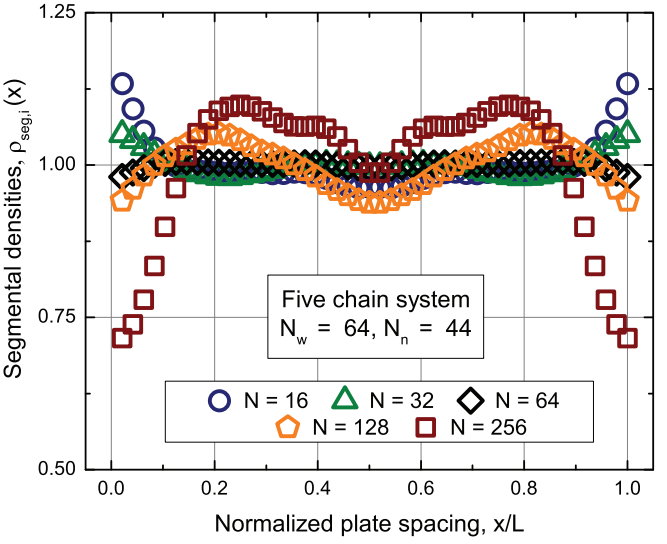

FIG. 7. (Color online) Segmental densities for the unentangled polydisperse system under quiescence.

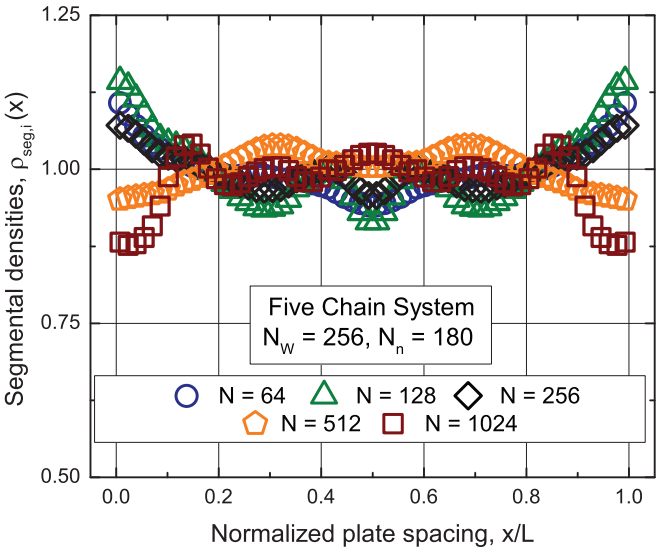

FIG. 8. (Color online) Segmental densities for the entangled polydisperse systems under quiescence.

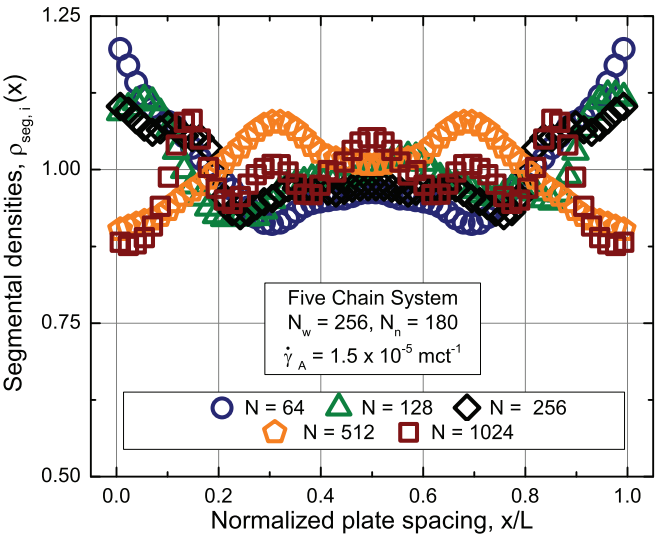

FIG. 10. (Color online) Segmental densities for the entangled polydisperse system under shear flow; segmental distributions are again very similar to the quiescent case (compare Fig. 8).

chains, comparison of Fig. 12 with Fig. 10 demonstrates the same strong migration effects. The longest chains in the simulations migrate to the midplane where the shear rate is lowest. The shorter chains are highly preferred near the wall. Unlike quiescence or shear flow, there is no recovery to a uniform distribution away from the wall near the center of the simulation box for the longest chains.

It is also observed that the excess of the longest chains at the midplane is proportional to the strength of the flow field. Figures 13 and 14 provide the normalized segmental density for the longest chains right next to the wall and at the midplane. As the wall shear rate is increased (equivalent to the flow rate or Reynolds number increasing), the excess of the longest chain segments at the midplane increases while those at the wall decrease. The difference in these two diverges as the Reynolds number increases. In contrast, values for the shear flow case correspond to the quiescent case up to the onset of wall slip (see velocity profiles in Figs. 3–6).

The simulations demonstrate that cross-flow migration effects are dominated by gradients in shear rate. The walls are nonenergetic and the system is at full occupancy meaning compressibility (free volume) does not play a role in these simulations (however, it is anticipated that in real polymer systems vacancies should migrate under flow). Under quiescent and simple shear conditions, shorter chains are preferentially located near the walls while the longer chains reside slightly away from the wall; further away from the walls, chains are nearly evenly distributed. This uniform distribution is approximated by the center of the simulation box for both

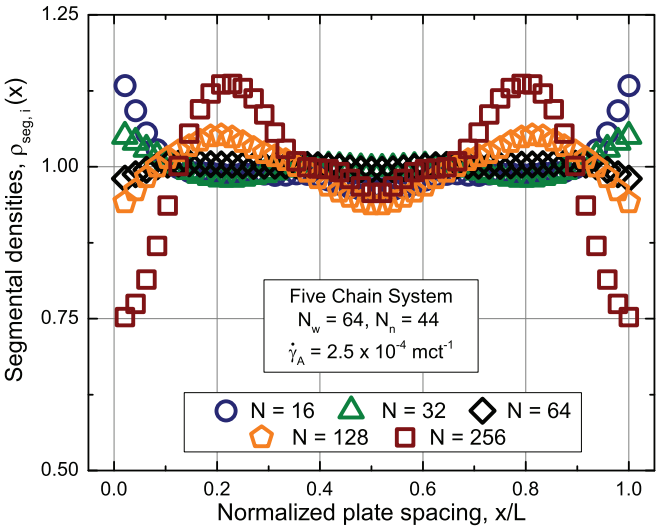

FIG. 9. (Color online) Segmental densities for the unentangled polydisperse system under shear flow; segmental distributions are very similar to the quiescent case (compare Fig. 7).

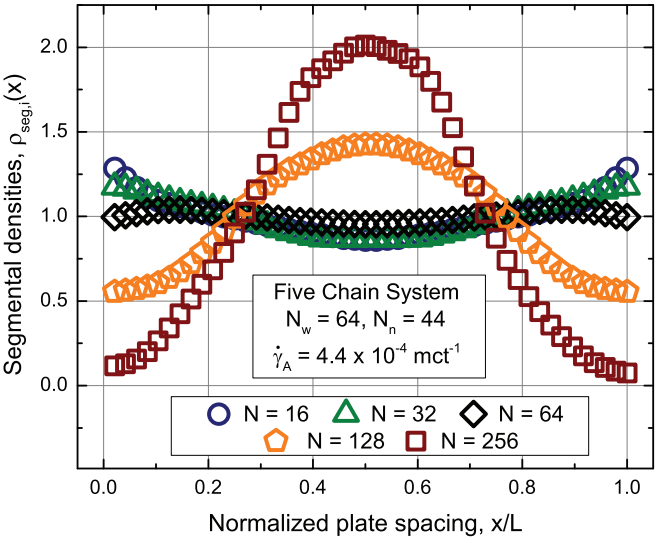

FIG. 11. (Color online) Segmental densities for the parabolic flow of an unentangled melt. Migration phenomena are clearly present upon comparison with Figs. 7 and 9 (note change in ordinate scale).

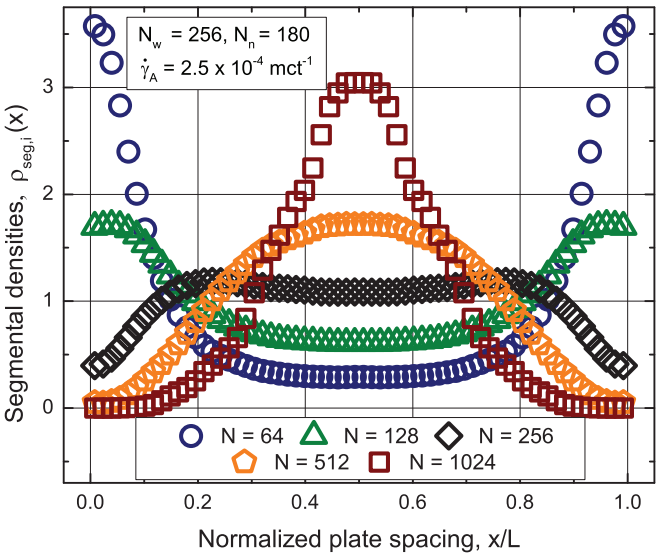

FIG. 12. (Color online) Segmental densities for the polydisperse entangled system under parabolic flow; length-based migration phenomenon is clearly present in comparison to Figs. 8 and 10 (note change in ordinate scale).

quiescence and shear flow. In contrast, when subjected to parabolic flow, very strong migration phenomena are present at all flow rates. The longest chains in the melt migrate to the midplane where the shear rate is lowest. Similarly, the shortest chains migrate to the wall where the shear rate is highest. The excess of longest chain segments at the midplane compared to the wall is proportional to the Reynolds number (equivalent to flow rate or wall shear rate). Since all simulations are conducted in the athermal limit, the migration phenomena are based purely on entropic factors.

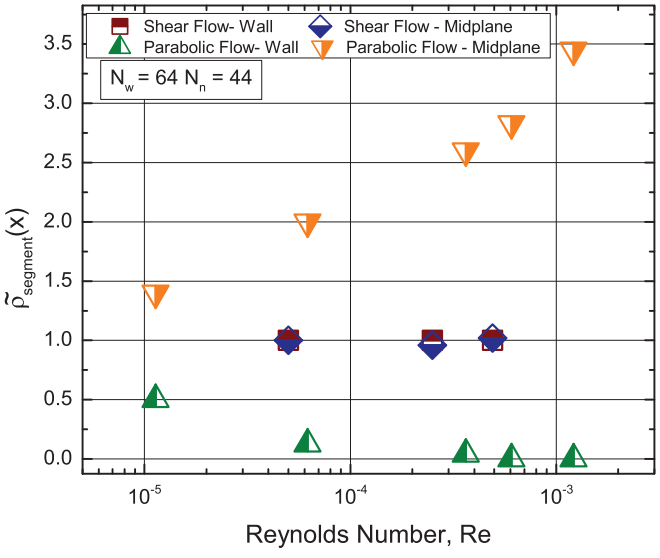

FIG. 13. (Color online) Normalized segmental densities for the unentangled case. Parabolic flow shows dramatic segregation whereas shear flow mimics quiescent conditions. It is the curvature of the deformation gradient that drives migration.

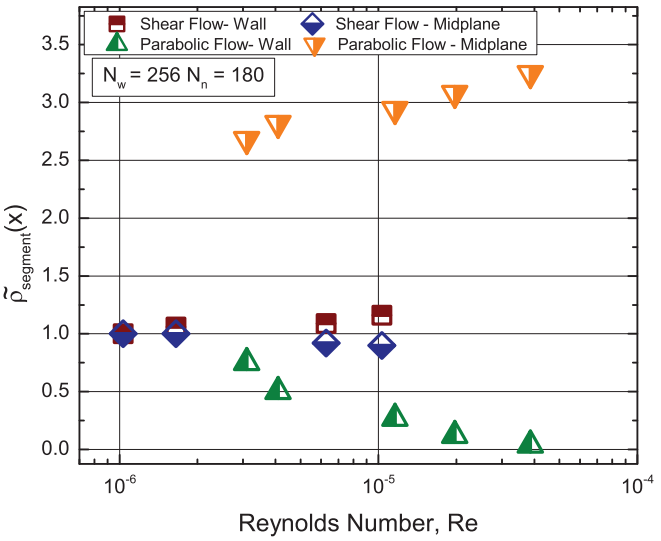

FIG. 14. (Color online) Normalized segmental density of the longest chains ($N = 1024$) in the entangled system for a wide range of Re numbers in shear and parabolic flow up to the point of cohesive failure. Before the onset of cohesive failure, there is no migration in shear flow, however, migration is present at all Re numbers in parabolic flow.

1. *Maximum stresses*

In the implementation of this Dynamic Monte Carlo technique the shear stresses range from 10^{-5} to 10^{-3} Π. This converts to a real stresses in the range 10^5–10^7 Pa. This stress is less than the stress required to break a carbon-carbon bond. Spectra, a commercial grade ultrahigh molecular weight polyethylene fiber, has an ultimate tensile strength of 3.7 GPa. This value is expected to be some fraction of the strength of the actual chemical bonds and yet far exceeds (by two orders of magnitude) the stresses reached in our simulations. Accordingly, the critical stress required to break a carbon-carbon bond is not obtained.

Similarly, a simple thought experiment can also be conducted in order to arrive at an estimate for the shear stress to break a bond. The work required to break the chemical bond is related to the energy of the bond. The equivalence of energy E and work W gives

$$E = W = Fd, \tag{27}$$

where F is the force required to stretch the bond a distance d. The energy of a CH_2-CH_2 bond is 88 kcal/mol [46]. The length of a carbon-carbon bond is approximately 1.54 Å. To break the bond we assume that it must be displaced by a distance of 1 Å. Using Eq. (14) and solving for force a value of 5×10^{-9} N is obtained. In order to get the stress, the force must be divided by a cross sectional area. In this example, for a single bond, the cross sectional area can be taken to be a circle of radius r, where the radius is twice the length of a carbon hydrogen bond. This results in a cross sectional area of 12.5 $Å^2$ and a stress of 37.1 GPa. This simple calculation suggests that spectra fibers achieve about 10% of the theoretically possible stress which is a reasonable gross approximation.

It can be concluded that the stresses achieved in the simulations are far lower than the stress required to break a carbon-carbon bond. Thus all results pertaining to slip, migration, and rheology are representative of systems in which stress-induced polymer degradation is not present. There is no need to invoke thermomechanical degradation to explain low molecular weight fractions on extrudate surfaces.

IV. CONCLUSIONS

All of the results presented in this study are consistent with ideas regarding the physical mechanisms governing nonequilibrium steady states. Namely, the system adopts the state of lowest free energy, or correspondingly, the system adopts a configuration in which *the entropy generation is minimized* [47]. Viscous dissipation per unit volume is calculated as the product of the shear rate with the shear stress or, given that the shear stress is the viscosity times the shear rate, as the viscosity times the shear rate squared. In parabolic flow, the shear rate is highest at the wall so if the system can arrange itself in a manner where lower viscosity components reside in the regions of highest shear rate, entropy generation is minimized. While it has been known for decades that in the capillary flow of high polymers shorter chains are found on the exterior of the extrudate, there has been controversy as to the mechanism being flow migration [22,23,26,27] or thermomechanical degradation [24,25]. The present simulations resolve this ambiguity by clearly demonstrating that cross-flow migration occurs in both unentangled and entangled polymer melts.

While chain length migration phenomena have been known for decades, the complexity involved has led to little theoretical consideration [14,17,18]. Incorporation of constitutive equations accounting for chain migration into computational fluids dynamics packages awaits implementation and poses significant challenges. Accordingly, while the present approach is limited to rather simplistic flow fields, the quantitative nature of the simulations holds significant promise for developing the detailed understanding needed for many potential technologies. Among the most prominent is next-generation DNA sequencing technologies [6]. Clearly the present simulations show that a melt of polymer chains can be fractionated according to molecular weight by dividing a pressure driven flow into smaller channels. Repeated division provides, in principle, arbitrary resolution in the precision of separation. While presented for polydisperse melts, the same cross-flow phenomenon is expected to hold for concentrated solutions of DNA of varying lengths.

ACKNOWLEDGMENT

This work was funded by the National Science Foundation under the Fluid Dynamics Program Grant No. CBET-1067707.

[1] M. Tirrell and M. F. Malone, J. Polym. Sci., Polym. Phys. Ed. **15**, 1569 (1977).
[2] U. S. Agarwal, A. Dutta, and R. A. Mashelkar, Chem. Eng. Sci. **49**, 1693 (1994).
[3] A. Metzner, Y. Cohen, and C. Rangel-Nafaile, J. Non-Newtonian Fluid Mech. **5**, 449 (1979).
[4] K. A. Dill and B. H. Zimm, Nucleic Acids Res. **7**, 735 (1979).
[5] M. D. Graham, Annu. Rev. Fluid Mech. **43**, 273 (2011).
[6] E. R. Mardis, Nature (London) **470**, 198 (2011).
[7] X. J. Fan, N. Phan-Thien, N. T. Yong, X. H. Wu, and D. Xu, Phys Fluids **15**, 11 (2003).
[8] R. M. Jendrejack, J. J. de Pablo, and M. D. Graham, *Iccn 2002: International Conference on Computational Nanoscience and Nanotechnology* (Nano Science and Technology Institute, Austin, TX, 2002), p. 111.
[9] R. M. Jendrejack, E. T. Dimalanta, D. C. Schwartz, M. D. Graham, and J. J. de Pablo, Phys. Rev. Lett. **91**, 038102 (2003).
[10] R. M. Jendrejack, D. C. Schwartz, and J. J. de Pablo, J. Chem. Phys. **120**, 2513 (2004).
[11] R. Khare, M. D. Graham, and J. J. de Pablo, Phys. Rev. Lett. **96**, 224505 (2006).
[12] J. Baschnagel, W. Paul, V. Tries, and K. Binder, Macromolecules **31**, 3856 (1998).
[13] J. P. Hernandez-Ortiz, J. J. de Pablo, and M. D. Graham, Phys. Rev. Lett. **98**, 140602 (2007).
[14] A. N. Beris and V. G. Mavrantzas, J. Rheol. **38**, 1235 (1994).
[15] H. Ma and M. D. Graham, Phys. Fluids **17**, 083103 (2005).
[16] S. Tsouka, Y. Dimakopoulos, V. Mavrantzas, and J. Tsamopoulos, J. Rheol. **58**, 911 (2014).
[17] M. Doi and A. Onuki, J. Phys. **2**, 1631 (1992).
[18] A. Elafif, M. Grmela, and G. Lebon, J. Non-Newtonian Fluid Mech. **86**, 253 (1999).
[19] W. F. Busse, Phys. Today **17**(9), 32 (1964).
[20] W. F. Busse, J. Polym. Sci., Part A: 2 Polym. Phys. **5**, 1261 (1967).
[21] G. Segré and A. Silberberg, Nature (London) **189**, 209 (1961).
[22] H. P. Schreiber and S. H. Storey, J. Polym. Sci., Part B: Polym. Lett. **3**, 723 (1965).
[23] H. Schreiber, S. Storey, and E. Bagley, Trans. Soc. Rheol. **10**, 275 (1966).
[24] L. R. Whitlock and R. S. Porter, J. Polym. Sci., Part B: 2 Polym. Phys. **10**, 877 (1972).
[25] L. R. Whitlock and R. S. Porter, J. Appl. Polym. Sci. **17**, 2761 (1973).
[26] B. L. Lee and J. L. White, Trans. Soc. Rheol. **18**, 467 (1974).
[27] B. L. Lee and J. White, Trans. Soc. Rheol. **19**, 481 (1975).
[28] J. Musil and M. Zatloukal, Chem. Eng. Sci. **81**, 146 (2012).
[29] Y. W. Inn, J. Rheol. **57**, 393 (2013).
[30] J. R. Dorgan, N. A. Rorrer, and C. M. Maupin, Macromolecules **45**, 8833 (2012).
[31] S. S. Gleiman and J. R. Dorgan, J. Chem. Phys. **112**, 6073 (2000).
[32] S. Geyler, T. Pakula, and J. Reiter, J. Chem. Phys. **92**, 2676 (1990).
[33] N. A. Rorrer and J. R. Dorgan, Macromolecules **47**, 3185 (2014).

[34] J. R. Dorgan and N. A. Rorrer, Phys. Rev. Lett. **110**, 176001 (2013).
[35] R. S. Pai-Panandiker, J. R. Dorgan, and T. Pakula, Macromolecules **30**, 6348 (1997).
[36] D. S. Pearson, L. J. Fetters, W. W. Graessley, G. Ver Strate, and E. von Meerwall, Macromolecules **27**, 711 (1994).
[37] K. F. Mansfield and D. N. Theodorou, Macromolecules **22**, 3143 (1989).
[38] M. Kotelyanskii and D. N. Theodorou, *Simulation Methods for Polymers* (Marcel Dekker, New York, 2004).
[39] H. Tao, T. P. Lodge, and E. D. von Meerwall, Macromolecules **33**, 1747 (2000).
[40] K. Jordens, G. L. Wilkes, J. Janzen, D. C. Rohlfing, and M. B. Welch, Polymer **41**, 7175 (2000).
[41] J. M. Dealy and K. F. Wissburn, *Melt Rheology and its Role in Plastics Processing* (Van Nostrand Reinhold, New York, NY, 1990).
[42] M. M. Denn, Annu. Rev. Fluid Mech. **33**, 265 (2001).
[43] S. G. Hatzikiriakos, Prog. Polym. Sci. **37**, 624 (2012).
[44] V. S. Minnikanti, Z. Qian, and L. A. Archer, J. Chem. Phys. **126**, 144905 (2007).
[45] D. T. Wu, G. H. Fredrickson, J. P. Carton, A. Ajdari, and L. Leibler, J. Polym. Sci., Part B: Polym. Phys. **33**, 2373 (1995).
[46] R. T. Morrison and R. N. Boyd, *Organic Chemistry* (Allyn and Bacon, Boston, 1983).
[47] P. Glansdorff and I. Prigogine, Physica (Amsterdam) **30**, 351 (1964).